Effects of terrain and landmass near Fujian Province of China on the structure and propagation of a long-lived rainband in Typhoon Longwang (2005): A numerical study

Yuanlong Li[1,2], Yuqing Wang[2, 3*], Yanluan Lin[1], Rong Fei[3,2], and Jianyun Gao[4]

[1]Ministry of Education Key Laboratory for Earth System Modeling, Department of Earth System Science, and Joint Center for Global Change Studies (JCGCS), Tsinghua University, Beijing, China.

[2]International Pacific Research Center and Department of Atmospheric Sciences, School of Ocean and Earth Science and Technology, University of Hawaii at Mānoa, Honolulu, Hawaii, USA.

[3]State Key Laboratory of Severe Weather, Chinese Academy of Meteorological Sciences, China Meteorological Administration, Beijing, China.

[4]Fujian Key Laboratory of Severe Weather, Meteorological Bureau of Fujian Province, China Meteorological Administration, Fuzhou, China

Jun 26, 2020 (Submitted)

August 17, 2020 (Revised)

Dateline

Key Points:

1. The studied long-lived rainband was locked up near the China coastline mainly due to the effect of land-sea surface roughness contrast.
2. The inland agradient force and surface friction helped maintain the rainband near the coastline by enhancing moisture convergence.
3. The terrains with low elevation and scattered distribution are shown to enhance the effect of land-sea surface roughness contrast.

Submitted to ***Journal of Geophysical Research – Atmospheres***

[*]Corresponding author address:
Prof. Yuqing Wang
International Pacific Research Center
University of Hawaii at Manoa
404A/POST, 1680 East West Road,
Honolulu, HI 96822, USA.
Email: yuqing@hawaii.edu

Abstract

A ~14-hr long-lived spiral rainband in Typhoon Longwang (2005) produced catastrophic rainfall in Fujian Province of China on 2 October 2005. In this study, the effects of terrain and landmass near Fujian on the structure and propagation of this rainband are investigated through high-resolution numerical simulations. Results show that although the terrain and landmass near Fujian played a marginal role in the formation of the rainband, both greatly affected the structure and propagation of the rainband. Namely, convection in the upwind sector of the rainband tended to be maintained and locked up near the coastline in the control experiment with both the terrain and landmass near Fujian retained, but shrank more inland with the terrain near Fujian flattened, and further inland with the landmass near Fujian replaced by the virtual ocean. It is found that due to the land-sea surface roughness contrast, the upstream tangential winds from ocean would be substantially decelerated over land and thus induced a local subgradient force onshore near the coastline. The radially inward agradient force and the subsequent surface friction helped maintain the moisture convergence, and thus convection and the cold pool in the upwind sector of the rainband near the coastline. Although the orographic lifting and blocking effects were found to be marginal to the moisture convergence in the rainband, the terrains near Fujian enhanced the deceleration of surface winds, enhancing the effect of land-sea surface roughness contrast on low-level moisture convergence and thus the lockup of the upwind sector of the rainband.

Plain Language Summary

A ~14-hr long-lived spiral rainband in Typhoon Longwang (2005) produced catastrophic rainfall in Fujian Province of China on 2 October 2005. The effects of terrain and landmass near Fujian on the structure and propagation of this rainband are investigated through high-resolution numerical simulations in this study. We show that although the terrain and landmass near Fujian played a marginal role in the formation of the rainband, both greatly affected the structure and propagation of the rainband. It is found that due to the land-sea surface roughness contrast, the upstream tangential winds from ocean were substantially decelerated over land and thus induced a local subgradient force onshore near the coastline. The radially inward agradient force and the subsequent surface friction helped maintain the moisture convergence, and thus convection and the cold pool in the upwind sector of the rainband near the coastline. Although the orographic lifting and blocking effects were found to be marginal to the moisture convergence in the rainband, the terrains near Fujian enhanced the deceleration of surface winds, enhancing the effect of land-sea surface roughness contrast on low-level moisture convergence and thus the lockup of the upwind sector of the rainband.

1. Introduction

Spiral rainbands are among the most striking components of a tropical cyclone (TC, also known as typhoon and hurricane). By bringing severe weathers, such as torrential rain, squalls, and tornadoes, spiral rainbands in landfalling TCs frequently lead to widespread destruction, property damage, and loss of life in geologically susceptible areas (e.g., Smith et al. 2009; Hall et al. 2013; Liu and Smith 2016; Lin et al. 2018). Because of insufficient understanding of the involved complex dynamical and physical processes, forecasts of TC spiral rainbands and their associated extreme rainfall are not always skillful and remain challenging.

A fascinating long-lived rainband formed onshore near the coast of Fujian Province of China in Typhoon Longwang (25 September to 3 October 2005), as Longwang approached Fujian Province from the southeast after it passed over Taiwan Island (Fig. 1). The rainband lasted for ~14 h and caused the most devastating rainfall in Fujian Province over the last 50 years, with a record-breaking hourly rainfall of 152 mm in Changle, Fujian (Lin et al. 2018). Unfortunately, the severe rainfall associated with this rainband was significantly underpredicted and 96 deaths were reported. Based on the available Doppler radar and surface observations, Lin et al. (2018) hypothesized that this rainband was induced by a previously existing wavenumber-2 vortex Rossby wave. Li et al. (2019) further verified this hypothesis using a high-resolution simulation and showed that the cold-pool dynamics and environmental vertical wind shear-induced wavenumber-1 forcing also played important roles in the maintenance of such a long-lived rainband. Another striking feature of this rainband, which was not addressed in either Lin et al. (2018) or Li et al. (2019), was that the rainband propagated along the coastline of Fujian Province away from the typhoon center. For such a long-lived rainband, in addition to its formation and maintenance, an accurate forecast of its propagation is also crucial for disaster risk prevention. Many previous observational studies have reported that spiral rainbands that form onshore of an approaching TC tend to be locked up near the coastline (e.g., Gao et al. 2009; Xu et al. 2014; Bao et al. 2015; Liu and Smith 2016). Most of those studies, including Lin et al. (2018) and Li et al. (2019), have attributed this phenomenon to the topographic effects or the differential friction between land and sea due to land-sea roughness contrast. However, the hypothesized mechanisms have not been discussed in detail.

The interaction between terrain/topography or landmass and onshore rainfall/rainbands of an approaching TC has been extensively investigated. Generally, for relative large mountains, such as the Central Mountain Range over Taiwan Island, TC rainfall is often largely affected by the orographic effects of the mountain through orographic blocking-induced structure change of rainbands (e.g., Yu and Tsai 2017; Lentink et al. 2018), orographic lifting-induced convection enhancement (e.g., Lin et al. 2002; Yu and Cheng 2013; Liu et al. 2016), and precipitation enhancement due to collision and coalescence processes between background raindrops of rainbands and orographic lifting-induced cloud water (i.e., the so-called seeder-feeder process; e.g., Smith et al. 2009; Yu and Cheng 2013). For the scattered, low, and small/mesoscale terrains, such as those in the coastal area of East China (with an average elevation of several hundred meters), the orographic effects on convection are marginal and TC rainfall is usually affected by the land-sea surface roughness contrast-induced convergence (e.g., Powell 1982; Li et al. 2014; Xu et al. 2014). Note that there are two effects associated with the land-sea surface roughness contrast on onshore convection. The first effect is the reduction of onshore winds over land due to the enhanced surface friction that can induce a low-level convergence onshore directly (e.g., Li et al. 2014). The second effect is the tangential deceleration of onshore winds over land that can cause a subgradient force and thus enhance the radial convergence in spiral rainbands (e.g., Powell 1982, Xu et al. 2014). Note that although the direct orographic effects of relatively low scattered terrains are marginal as mentioned above, they may still affect rainbands/rainfall by decelerating the surface winds and thus enhancing low-level convergence. The latter has not been studied in any detail in the literature. In addition, most of previous studies on the interaction between terrain/landmass and rainfall/rainbands of a TC have focused primarily on the transient local rainfall. How terrain and landmass may affect the propagation of a previously existing long-lived rainband has not been previously investigated.

The objective of this study is to address the above issues using the high-resolution simulation results of Typhoon Longwang (2005) by Li et al. (2019), in which the simulated rainband also showed a long-lived feature and propagated near the Fujian coastline as in observation. To understand different effects of the terrain and landmass near Fujian on convection, in addition to the control experiment of Li et al. (2019), two sensitivity experiments were conducted by flattening the terrain near Fujian and replacing the land near Fujian by ocean, respectively. The experimental design is described in Section 2, and the results are discussed in Section 3. The detailed mechanisms of how the terrain and landmass near Fujian affect the structure and propagation of the rainband are analyzed in Section 4. The major conclusions are summarized in Section 5.

2. Experimental design

The Advanced Research Weather Research and Forecasting model (WRF), version 3.8.1 (Skamarock et al. 2008), was used to simulate Typhoon Longwang (2005). The model settings of the control experiment in this study, including the physical parameterizations and initialization, were identical to those used in Li et al. (2019). The model domain was triply nested with horizontal grid spacings of 12, 4, and 1.33 km, respectively, as shown in Fig. 1a. The inner two meshes automatically moved following the typhoon center at 500 hPa. There were 36 uneven vertical levels with the model top at 50 hPa, and with the low-level grid spacing approximately stretched from 56.6 m near the surface to 380 m at 2500 m. The model was integrated from 0000 UTC 30 September 2005 to 1800 UTC 2 October 2005 with the initial and lateral boundary conditions interpolated from the National Centers for Environment Prediction Global Forecast System Final Analysis (GFS-FNL), which had a horizontal grid spacing of $1^{o}\times1^{o}$. The dynamical initialization scheme (Cha and Wang 2013) was used on the outermost mesh to improve the initial conditions of the targeted typhoon, with the outputs of sea level pressure and surface circulation shown in Fig. 1a. The initial conditions on the inner two meshes were interpolated from the outermost mesh at the end of dynamical initialization. The spectral large-scale nudging (Von Storch et al. 2000) was applied to the horizontal wind field in the outermost domain to reduce the model biases in reproducing the large-scale circulation field.

Three experiments with different underlying surface conditions were conducted to examine the roles of terrain and landmass near Fujian on the propagation of the rainband. In the control experiment (CTL), both the terrain and landmass were retained. In the first sensitivity experiment (FLT), the terrain near Fujian in the coastal area of Mainland China south of 28ºN and east of 114.5ºE (outlined in orange dashed lines in Fig. 1a and zoomed in Fig. 2a) was flattened, namely, with the terrain height set to zero in the input data before the integration of simulation. This area was chosen because it contains the total body of the rainband of interest in the control experiment (cf. Figs. 2b–d). In the second sensitivity experiment (OCN), the land near Fujian in the same area for terrain removal in the first sensitivity experiment was replaced by the virtual ocean, and the sea surface temperature of the virtual ocean was fixed as the averaged sea surface temperature in the nearby Taiwan Strait. Note that our preliminary tests indicate that the overall conclusions discussed herein are insensitive to the size of the area and the virtual sea surface temperature in reasonable ranges (not shown). As in CTL, the two sensitivity experiments were also integrated from 0000 UTC 30 September 2005 to 1800 UTC 2 October 2005.

It is worth pointing out that there are two methods to treat terrain in the moving inner meshes in WRF. One is the default method, by which terrains in the two moving inner meshes are interpolated from the outermost mesh, as used in Li et al. (2019) or in CTL. In this case, the resolutions of terrains in all three meshes are 12 km. In the other method (Chen et al. 2007), terrains in the two moving inner meshes are interpolated from the basic high-resolution topographic dataset from the US Geological Survey. To address whether the resolution of the terrain near Fujian would affect our results in CTL, we conducted an extra experiment as CTL (Figs. 2b–d) but using the high-resolution terrain dataset based on the second method (Figs. 2f–h), with the terrains near Fujian in the innermost mesh by the two methods shown in Figs. 2a and 2e. Note that to reduce the influence of different resolutions of terrains over Taiwan Island in this comparison, the high-resolution terrain experiment was activated from 0200 UTC 2 October, namely prior to the formation of the rainband of interest and after Typhoon Longwang passed Taiwan Island, using the restart files from CTL. Although the higher resolution terrain experiment could show a more detailed convective structure (Rivera-Torres 2018), we found that the overall structure and evolution of the rainband, which are our focus in this study, are similar in the two experiments (Figs. 2b–d, 2f–h). Therefore, for simplicity, the terrains in the two inner meshes are interpolated from the outermost mesh in all three experiments.

3. Results

The TC track, maximum surface wind speed, and minimum sea level pressure from the three experiments are compared in Fig. 1, superimposed upon the best track data from the China Meteorological Administration, which were obtained from the International Best Track Archive for Climate Stewardship (IBTrACS; Knapp et al. 2010). The modeled tracks in the three experiments are all similar to the track from IBTrACS (Fig. 1a). The simulations captured the first landfall over Taiwan Island and the second landfall over Fujian Province but the landfall times were about 3 and 7 hours earlier than the observed for the first and the second landfalls, respectively, due to the faster translational speed of the simulated storms after 1200 UTC 1 October (Fig. 1a). The faster translational speed of the simulated storms was related to the model errors in the simulated environmental steering flow (not shown). The overall intensity evolutions of the three simulated storms were similar to that in IBTrACS except for a large positive intensity bias in the simulations before 0000 UTC 1 October (Fig. 1b). In addition, the simulated storm was stronger during and after its landfall over Fujian (~0800 UTC 2 October) in OCN than in CTL and IBTrACS and a little stronger in FLT than in CTL (Fig. 1b). The results suggest that both the track and intensity of the storm were marginally affected by the terrain near Fujian, and the weakening of the storm after landfall was mainly caused by the landmass.

Figure 3 shows the evolutions of the simulated rainband of interest in all three experiments (Figs. 3a2–f2, 3a3–f3, and 3a4–f4) and the observed rainband in the Doppler radar reflectivity images (Figs. 3a1–f1) from the Central Weather Bureau (CWB). A similar rainband can be found in all three experiments, suggesting that the formation of the rainband was not affected by the terrain or landmass near Fujian. Note that the simulated rainband in all three experiments formed around 0220 UTC 2 October (not shown, cf. Li et al. 2019), about 5 hours earlier than the observed (cf. Figs. 3a1–b1, 3a2–b2, 3a3–b3, and 3a4–b4), which seems partly due to the faster movement of the simulated storms than that of the observed (Fig. 1a). As discussed in Li et al. (2019), the formation of the rainband in CTL was closely related to a preexisting wavenumber-2 potential vorticity wave (Figs. 4a–c). The same signal was also found in FLT (Figs. 4d–f) and OCN (Figs.

4g–i). Based on the calculated propagation speed of this wave, Li et al. (2019) found that the rainband in the early stage in CTL showed a characteristic of convectively coupled vortex Rossby wave (cf. Wang 2002). Here, we found that the wavenumber-2 wave propagated cyclonically in the azimuth and radially outward and showed similar propagation speeds in the three experiments. This means that the formation of the rainband among the three experiments was similar and was triggered by a preexisting convectively coupled wavenumber-2 vortex Rossby wave (Li et al. 2019). A detailed description about the evolution of the observed rainband and the simulated rainband in CTL can be found in Lin et al. (2018) and Li et al. (2019), respectively. Here, we mainly focus on the propagation of the rainbands.

In CTL, before 0600 UTC 2 October, the simulated rainband had formed north of the typhoon center and was characterized by an inner spiral rainband (Figs. 3b2, c2; Li et al. 2019). Namely, the rainband was close to the eyewall and organized in an azimuthally elongated banded pattern (e.g., Wang 2008; Li et al. 2017). Subsequently, the rainband propagated radially outward, showing a wavenumber-1 structure featured as an outer rainband or a principal rainband (Figs. 3d2–f2) with stratiform precipitation in the downwind sector connected with the inner core and strong convection and convective cells in the upwind sector (e.g., Wang 2008; Li et al. 2017). The upwind sector of the rainband is the focus of this study because it caused the record-breaking rainfall along the coast of Fujian (Lin et al. 2018; Li et al. 2019). We can see that the upwind sector of the simulated rainband propagated anticyclonically relative to the storm center and remained near the coastline (Figs. 3d2–f2; Li et al. 2019), similar to that of the observed rainband (Figs. 3d1–f1) although the simulated rainband was more inland than the observed after ~1000 UTC 2 October.

In FLT and OCN experiments, the rainband was due north of the typhoon center and near the eyewall before 0600 UTC 2 October (Figs. 3b3–c3, 3b4–c4), similar to that in CTL (Figs. 3b2–c2). However, later on, although the rainband in the two sensitivity experiments showed a wavenumber-1 structure as in CTL (Figs. 3d2–f2, 3d3–f3, and 3d4–f4), some differences became obvious. The upwind sector of the rainband in CTL stayed near the coastline, thus showing an apparent anticyclonic propagation from the due north of the typhoon center at 0600 UTC (Fig. 3c2) to the northeast at 0800 UTC (Fig. 3d2). However, the upwind sector of the rainband in the two sensitivity experiments propagated inland, showing a cyclonic rotation from the due north (Figs. 3c3-d3, 3c4-d4) to the northwest of the typhoon center (Figs. 3e3-f3, 3e4-f4). Convection in the middle and downwind sectors of the rainband was stronger in FLT (Figs. 3d3–f3) than in CTL (Figs. 3d2–f2), and even stronger in OCN (Figs. 3d4–f4). Therefore, it seems that both the terrain and landmass near Fujian played important roles in the propagation and structure of the rainband.

To further show the detailed differences in the propagation and structure of the rainband among the three experiments, we plot in Fig. 5 the 10-h accumulated precipitation during 0300–1300 UTC 2 October over Fujian in the three experiments, overlaid with the observations during 0800–1800 UTC 2 October from rain gauges. Note that the 5-hour shift between observations and simulations for the comparison reflects the earlier arrival of the simulated rainband than the observed because of the faster translational speed of the simulated storms as mentioned above. Although with a slight shift in the area of the maximum precipitation, the observed local rainfall area along the coast of Fujian Province with the accumulated precipitation over 50 mm was reproduced reasonably well in CTL (Fig. 5a). Note that the maximum accumulated precipitation was also near the coastline in the two sensitivity experiments, but it was mainly contributed by convection in the eyewall and the secondary rainband rather than the rainband of interest (not shown, cf. Figs. 3b3–f3, 3b4–f4). The two sensitivity experiments did not capture the rainfall pattern well. The 50-mm rainfall contour on the west side appears more inland in FLT than in CTL, and further inland from FLT to OCN. The discrepancy in the overall accumulated rainfall distribution is consistent with the more inland upwind sector of the rainband and the more evenly spread convection along the rainband in the two sensitivity experiments as discussed above (Fig. 3).

4. Interpretation

In the last section, we show that both the terrain and landmass near Fujian played important roles in affecting the propagation of the rainband of interest, especially its upwind sector. To understand how the terrain and landmass modulated the rainband propagation, in this section, we will first discuss the maintenance mechanism of convection in the upwind sector of the rainband and then analyze the orographic effects and the effect of land-sea surface roughness contrast on convection of the rainband.

4.1. The maintenance mechanisms of the rainband

Li et al. (2019) have shown that the rainband (upwind sector) after ~0600 UTC 2 October in

CTL was maintained by the cold pool dynamics and the environmental vertical wind shear. It is our interest to understand the differences in the maintenance mechanism of the rainband in the two sensitivity experiments from that in CTL. Figure 6 shows the virtual potential temperature at 900 hPa, the radar reflectivity at 3-km height, and deep-layer vertical wind shear between 200 and 700 hPa during 0400–1000 UTC 2 October in the three experiments. We can see from Fig. 6 that there was no obvious surface cold pool under the rainband prior to 0600 UTC in all three experiments (Figs. 6a,e,i), but a small and weak cold pool appeared in the upwind sector of the rainband around 0600 UTC (red arrows in Figs. 6b,f,j) and the surface cold pool strengthened later (Figs. 6c,g,k). Based on the Rotunno-Klemp-Weisman theory (Rotunno et al., 1988), the intensity of the cold pool can be estimated as (e.g., Lin et al. 2018; Li et al. 2019)

$$C = \sqrt{g \frac{\Delta\theta_v}{\theta_{v0}} H_c}, \tag{1}$$

where g is the gravitational acceleration, $\Delta\theta_v$ is the virtual potential temperature perturbation associated with the cold pool, θ_{v0} is the environmental virtual potential temperature, and H_c is the cold pool depth. From Figs. 7a,c,e and Figs. 6c,g,k, $\Delta\theta_v$ and θ_{v0} near the upwind sector of the rainband at 0800 UTC in all three experiments were ~1.5–2 ºC and ~306–308 ºC, respectively. The cold pool depth was ~2–3 km (Figs. 7a,c,e), this yields an intensity of the cold pool about 10–14 m s^{-1}, which balanced well the corresponding low-level cross-band vertical shear of ~10–15 m s^{-1} to the front of the cold pool (Figs. 7a,c,e). This strongly suggests that the surface cold pool dynamics played an important role in the maintenance of convection in the upwind sector of the rainband in the three experiments (Figs. 6c,g,k).

After 0800 UTC, the cold pool near the coastline in the upwind sector of the rainband in CTL weakened (Fig. 7b) and moved slightly inland (Fig. 6d), which corresponded with the inland shift of the simulated rainband compared with the observed (Figs. 3e1–f1, 3e2–f2). Nevertheless, from Fig. 7b, the weakened cold pool ($\Delta\theta_v \sim 1$ °C, $H_c \sim 2$ km) near the coastline in the upwind sector of the rainband in CTL still had an intensity (~8 m s^{-1}) sufficiently to balance the low-level cross-band vertical shear of ~10 m s^{-1} to the front of the cold pool. Unlike that in CTL (Fig. 6d), the cold pool in the two sensitivity experiments weakened very rapidly after 0800 UTC, and the cold pool under the upwind sector of the rainband disappeared by around 1000 UTC (Figs. 6g–h, 6k–l, Figs. 7d,f), consistent with the continued weakening and more inland shrinking of convection in the upwind sector of the rainband (Figs. 6g–h, 6k–l) compared with that in CTL (Fig. 6d). These results further confirm the importance of the surface cold pool dynamics to the maintenance of convection in the upwind sector of the rainband in all three experiments. Although there was also no cold pool in the middle and downwind sectors of the rainband in the two sensitivity experiments, convection was still maintained for several hours partly in response to the environmental vertical shear of horizontal winds averaged in an annulus between radii 200 km and 800 km from the storm center between 200 and 700 hPa (Figs. 6h,l) or between 1–6 km height (not shown). Previous studies have already shown that deep-layer vertical wind shear can induce convection in the downshear and downshear-left quadrants of a TC (e.g., Wang and Holland 1996; Frank and Ritchie 2001; Li et al. 2017). In addition, because there was no obvious difference in both direction and magnitude of the deep-layer vertical wind shear at the later stage among the three experiments (Figs. 6c–d, 6g–h, and 6k–l), the weakening of convection in the upwind sector of the rainband in the two sensitivity experiments was not related to the deep-layer vertical wind shear.

To understand why convection and cold pool in the upwind sector of the rainband failed to be maintained in the later stage without the terrain and/or landmass near Fujian, we show in Fig. 8 the low-level averaged horizontal water vapor flux and the corresponding convergence in the three experiments. In CTL (Figs. 8a–c), a local maximum in water vapor flux (and its convergence) appeared near the coastline. The convergence of water vapor flux (yellow contours; mostly under the red contours) was largely attributed to the convergence of horizontal wind (red contours) because the horizontal gradient of water vapor content was small near the coastline (not shown). Such a distinct local maximum in water vapor flux and its convergence near the coastline was hardly found in FLT (Figs. 8d–f), but the water vapor flux and its convergence, and thus convection in the middle and downwind sectors of the rainband were stronger in FLT (Figs. 8d–f, Figs. 3d3–f3) than in CTL (Figs. 8a–c, Figs. 3d2–f2). In OCN (Figs. 8g–i), the distributions of the water vapor flux and its convergence along the rainband became more uniform than in FLT (Figs. 8d–f), consistent with more uniform convection along the rainband in OCN (Figs. 3d4–f4) than in FLT (Figs. 3d3–f3). Therefore, both the terrain and landmass near Fujian contributed to the local maximum in water vapor flux convergence near the coastline and prohibited the inland transport of water vapor (Figs. 8a–c), favoring convection in the upwind sector of the rainband to be maintained along the coastline while suppressing convection in the middle and downwind sector of the rainband.

4.2. Orographic effects

Terrains can affect the convergence of water vapor flux by orographic lifting or/and blocking. The two effects can be distinguished by the Froude number (F_r; Smith 1979), i.e.,

$$F_r = \frac{U}{NH}, \tag{2}$$

where U is the upstream oncoming wind speed, H is the terrain height above sea level (ASL), and N is the Brunt-Väisälä frequency. For a given terrain height, weak low-level winds ($F_r < 1$) tend to be blocked by the terrain and thus induce a convergence on the windward side of the terrain. However, strong low-level winds ($F_r > 1$) tend to climb over the terrain but also can induce a convergence on the windward side if the slope of the terrain is steep (e.g., Lin et al. 2002; Yu and Cheng 2013; Liu et al. 2016). In the coastal region of Fujian Province, the maximum terrain height ASL is ~1000 m (Figs. 9d–i), and the averaged upstream wind speed and Brunt-Väisälä frequency near the rainband are ~20–30 m s^{-1} and ~1–1.5×10^{-2} s^{-1} (Figs. 9a–c). This gives a large Froude number ~1.5-3 and even larger for lower terrains. This suggests that the orographic blocking effect on convection in the rainband was marginal and the upstream wind from the ocean tended to climb over those terrains.

The orographic lifting effect can be quantified by the orographic lifting-induced upward water vapor flux (Smith 1979; Lin et al. 2002),

$$q_v w_{dia} = q_v |\vec{\boldsymbol{V}}| \frac{\partial H}{\partial s}, \tag{3}$$

where q_v, w, and $|\vec{\boldsymbol{V}}|$ are the low-level water vapor mixing ratio, vertical velocity, and total horizontal wind speed, and $\partial H/\partial s$ is the slope of the terrain along the direction of the total wind

s. The upward water vapor flux at 1000-m height ASL (results are insensitive to the height) was diagnosed and shown in Figs. 9d–f. The maximum in the diagnosed orographic lifting-induced water vapor flux (yellow contour) is only about 1/5 of that in the simulated water vapor flux in CTL (red contour). In addition, the orographic lifting-induced water vapor flux (yellow contour in Figs. 9d–f) was scattered following the terrains, while the simulated water vapor flux in CTL (red contour in Figs. 9d–f) shows a local maximum near the coastline as the water vapor convergence near the upwind sector of the rainband (Figs. 8a–c). This means that the orographic lifting effect also played a marginal role in the maintenance of convection in the upwind sector of the rainband and the propagation of the rainband. This is consistent with the statistical study of Xu et al. (2014), who found that the typhoon-induced precipitation along the coast of China was mainly caused by the land-sea surface roughness contrast rather than the orographic lifting because the terrains along the coast of China are low and scattered with small slope as shown in Figs. 9d–i.

Note that the seeder-feeder accretion mechanism associated with the orographic effect was not discussed in this study, not only because of the weak orographic lifting but also because it mainly contributes to convection on the leeward side of terrains (e.g., Smith et al. 2009; Yu and Cheng 2013) rather than on the windward side near the coastline.

4.3. Effect of land-sea surface contrast

Although the two orographic effects of the terrain near Fujian were marginal on convection in the rainband, the terrain slowed down the near-surface horizontal winds (cf. Figs. 9g–i), which could increase the near-surface vertical wind shear, thus enhancing vertical turbulent momentum mixing in the boundary layer. This may indirectly enhance the effect of land-sea surface contrast on convection near the coastline. As mentioned in the introduction, there are two effects of the land-sea surface roughness contrast on the water vapor convergence onshore near the coastline. One is associated with the direct deceleration of the windward total winds (Li et al. 2014), while the other is associated with the radially inward agradient force induced by the deceleration of windward tangential winds due to enhanced vertical turbulent mixing (Powell 1982). To examine the two effects, we show in Fig. 10 the radial and azimuthal components of the low-level water vapor flux and their corresponding convergences in CTL. We can see that the convergence in the rainband was mainly caused by the radial convergence (Figs. 10a–c), and a similar situation occurred in both FLT and OCN (not shown). This is probably because the orientation of the rainband was almost parallel to the onshore tangential winds. Note that although the water vapor flux was larger in the azimuthal direction than in the radial direction, the gradient of the water vapor flux, and thus the water vapor flux convergence, was lager in the radial direction than in azimuthal direction. This means that the water vapor convergence was largely contributed by the acceleration of radial winds, which was partly attributed to the inward agradient force associated with the deceleration of tangential winds, while the water vapor convergence directly induced by the deceleration of tangential winds was marginal.

To demonstrate the above-mentioned indirect effect, we compared the tangential wind tendency induced by vertical diffusion (mixing) of tangential wind (including surface friction) averaged between the surface and 1000-m height in the later stage of the rainband in the three experiments in Fig. 11. As analyzed earlier, the vertical mixing near the upwind sector of the rainband was larger in CTL (Figs. 11a–c) than in FLT (Figs. 11d–f) due to the presence of terrains therein in the former. As expected, although with a stronger low-level wind speed in OCN (cf. Fig. 1b), the vertical mixing near the upwind sector of the rainband was smaller in OCN (Figs. 11g–i) than FLT (Figs. 11d–f) because of the smaller surface roughness over ocean than over land. The large vertical mixing in the front (radially outside) of the rainband in CTL would decelerate the onshore tangential winds, inducing a radially inward agradient force therein. As a result, the inflow toward the region of the upwind sector of the rainband would be accelerated, leading to the enhanced water vapor convergence in the rainband. To further demonstrate this process, we calculated the agradient force near the rainband. The agradient force can be given as

$$Agr = fv + \frac{v^2}{r} - \frac{\partial \phi}{\partial r}, \tag{4}$$

where f is the Coriolis parameter, v is tangential wind speed, r is radius, and ϕ is geopotential on isobaric surface. Figures 12a–c show the averaged tangential wind speed and Figs. 12d-f show the averaged agradient force between 850–1000 hPa at 1000 UTC 2 October (results are similar at other times, not shown) near the upwind sector of the rainband (magenta rectangle in Figs. 11b,e,h) in the three experiments. As expected, partly due to the increased vertical diffusion (mixing) of tangential wind (Fig. 11b) and thus the reduction of onshore tangential winds in the front of the upwind sector of the rainband (highlighted by the red line in Fig. 12a), there was a large radially inward agradient force herein near the coastline of Fujian in CTL (Fig. 12d). In FLT, although there was a reduction of onshore tangential winds along the coast near the surface (not shown), the vertically integral-averaged reduction of onshore tangential winds was hardly found (Fig. 12b) and the agradient force was much reduced (Fig. 12e). In OCN, the reduction of onshore tangential winds was hardly found in each level (cf. Fig. 12c), and the agradient force shifted more inland with the rainband (Fig. 12f) than in CTL and FLT (Figs. 12d,e). This demonstrates that the deceleration of onshore tangential winds near the coastline in CTL induced a radially inward agradient force and thus acceleration of inflow (Powell 1982; Fig. 12j), which was contributed by both the terrain and landmass near Fujian.

Note the vertical mixing including surface friction of radial wind in the front of the upwind sector of the rainband increased partly as the radial wind accelerated in CTL (Fig. 12g), and was much larger than in FLT and OCN (Figs. 12h–i) also partly due to the presence of terrains and landmass. The increased vertical mixing of radial wind decelerated the radial wind on the inland side (Fig. 12j), enhancing the development of a large convergence of radial wind near the coastline in the rainband in CTL (Fig. 10). The increased vertical mixing of radial wind (Fig. 12g) was slightly radially inside of the radially inward agradient force (Fig. 12d). This means that in addition to the environmental radial wind, the radial wind accelerated by the radially inward agradient force in the front of the rainband could be partly decelerated by the radially outward radial wind tendency induced by vertical mixing including surface friction of radial wind. However, with the terrain flattened near Fujian or replaced by ocean in FLT or OCN, the agradient force, vertical mixing including surface friction of radial wind, and thus the radial convergence became much smaller and shifted inland than in CTL (Figs. 12d–l). As a result, convection in the rainband near the coastline continuously weakened during the late stage in FLT (Figs. 3d3–f3) and OCN (Figs. 3d4–f4). The above results strongly suggest that although the direct orographic effects of terrains near Fujian on convection were marginal, those low terrains played an important role in maintaining the low-level convergence and thus convection along the coastline by enhancing the effect due to the land-sea surface roughness contrast.

5. Conclusions and discussion

A long-lived rainband in Typhoon Longwang (2005) formed on 2 October 2005 near the coastline of Fujian and lasted for ~14 hours and brought about torrential rainfall in Fujian Province, China. The effects of terrain and landmass near Fujian on the rainband propagation and structure have been investigated based on numerical experiments using the WRF model. A control experiment with standard model settings captured well the overall track and intensity of the storm and the evolution and propagation of the rainband of interest. As discussed in Li et al. (2019), the formation of the rainband was associated with a preexisting wavenumber-2 potential vorticity wave, which showed a characteristic of vortex Rossby wave as in observation (Lin et al. 2018). In this study, we have found that although both the terrains and landmass near Fujian had little effects on the formation of the rainband, they largely modulated the propagation of the upwind sector of the rainband near the coastline at the later stage. This was demonstrated with results from two sensitivity experiments in which either the terrain near Fujian was flattened or the landmass near Fujian was replaced by ocean. In these two experiments, the upwind sector of the rainband moved inland away from the coastline and convection in the middle and downwind sectors became more evenly distributed and stronger than in the control experiment.

It is found that both the orographic lifting and blocking effects of the terrain near Fujian contributed marginally to the propagation of the rainband because of the low elevation, small slope, and scattered distribution of the terrains near Fujian. Instead, it was the water vapor convergence near the coastline due to the land-sea surface roughness contrast that contributed to the propagation of the upwind sector of the rainband. The sudden increase in surface friction onshore over land along the coastline decelerated the onshore tangential winds from the ocean, causing a radially inward agradient force and thus the acceleration of radial wind in the front of the rainband onshore near the coastline. The large radial winds were decelerated partly due to vertical mixing and surface friction inland, enhancing the convergence of radial wind, maintaining the moisture convergence near the coastline, and thus convection and cold pool in the upwind sector of the rainband onshore along the coastline. This process was largely enhanced by the presence of the terrain near Fujian. Note that partly because the orientation of the rainband was almost parallel to the onshore tangential winds, the convergence of tangential wind due to the enhanced surface friction-induced reduction of tangential wind was less important in maintaining the water vapor convergence in the rainband in this case. These results in general support the hypothesis of Lin et al. (2018) and Li et al. (2019), who suggested that the terrain and landmass near Fujian could play important roles in maintaining convection and cold pool in the upwind sector of the rainband by enhancing the local water vapor convergence near the coastline and prohibiting the inland transport of water vapor.

Results from this study demonstrate that the small and mesoscale terrains with low elevation and scattered distribution near the coastline played important roles in affecting the propagation and maintaining convection by enhancing the effect of land-sea surface roughness contrast. Note that although we showed that the overall structure and evolution of the rainband were insensitive to the resolution of the terrain near Fujian in the studied case, we should point out that adequately resolving the small and mesoscale terrains in numerical models is important for numerical prediction of rainfall associated with landfalling tropical cyclones. In addition, our main conclusions are reached based on one case study of the rainband in Typhoon Longwang, more rainband cases in landfalling TCs worldwide can be investigated to confirm the findings from this study and to examine the impact of terrains with different sizes and elevations on landfalling TC rainbands in the future.

Acknowledgments: IBTrACS data were downloaded from https://www.ncdc.noaa.gov/ibtracs/. WRF and WPS (WRF Preprocessing System) source code were downloaded from http://www2.mmm.ucar.edu/wrf/users/download/get_source.html, and the corresponding initial and lateral boundary conditions input to WPS were downloaded from https://www2.mmm.ucar.edu/wrf/users/download/free_data.html. The observed data including the radar reflectivity and precipitation, and all model data together with the model name-list are available at https://github.com/yuanlong-data/2020JGR-Longwang. This study has been supported in part by the National Key R&D Program of China under grants 2017YFC1501602, the National Natural Science Foundation of China under grant 41730960, and in part by the NSF grant AGS-1834300. Y. Li is funded by China Scholarship Council (File 201806210324) and R. Fei is funded by China Scholarship Council (File 201905330037). J. Gao is funded by the National Key Program for Developing Basic Science (2018YFC1505906).

References

Bao, X., N. E. Davidson, H. Yu, M. C. Hankinson, Z. Sun, L. J. Rikus, J. Liu, Z. Yu, and D. Wu, 2015: Diagnostics for an extreme rain event near Shanghai during the landfall of Typhoon Fitow (2013). *Mon. Wea. Rev.,* **143**, 3377–3405, doi:10.1175/MWR-D-14-00241.1.

Cha, D., and Y. Wang, 2013: A dynamical initialization scheme for real-time forecasts of tropical cyclones using the WRF model. *Mon. Wea. Rev*., **141**, 964–986, doi:10.1175/MWR-D-12-00077.1.

Chen, S. S., J. F. Price, W. Zhao, M. A. Donelan, and E. J. Walsh, 2007: The CBLAST-Hurricane program and the next-generation fully coupled atmosphere–wave–ocean models for hurricane research and prediction. *Bull. Amer. Meteor. Soc.,* **88**, 311–318, doi:10.1175/BAMS-88-3-311.

Frank, W. M., and E. A. Ritchie, 2001: Effects of vertical wind shear on the intensity and structure of numerically simulated hurricanes. *Mon. Wea. Rev.,* **129**, 2249–2269, doi:10.1175/1520-0493(2001)129<2249:EOVWSO>2.0.CO;2.

Gao, S., Z. Meng, F. Zhang, and L. F. Bosart, 2009: Observational analysis of heavy rainfall mechanisms associated with severe Tropical Storm Bilis (2006) after its landfall. *Mon. Wea. Rev*., **137**, 1881–1897, doi:10.1175/2008MWR2669.1.

Hall, J. D., M. Xue, L. Ran, and L. M. Leslie, 2013: High-resolution modeling of Typhoon Morakot (2009): Vortex Rossby waves and their role in extreme precipitation over Taiwan. *J. Atmos. Sci.*, **70**, 163–186, doi:10.1175/JAS-D-11-0338.1.

Knapp, K. R., M. C. Kruk, D. H. Levinson, H. J. Diamond, and C. J. Neumann, 2010: The International Best Track Archive for Climate Stewardship (IBTrACS) unifying tropical cyclone data. *Bull. Amer. Meteor. Soc*., **91**, 363–376, doi:10.1175/2009BAMS2755.1.

Lentink, H. S., C. M. Grams, M. Riemer, and S. C. Jones, 2018: The effects of orography on the extratropical transition of tropical cyclones: A case study of Typhoon Sinlaku (2008). *Mon. Wea. Rev.*, **146**, 4231–4246, doi:10.1175/MWR-D-18- 0150.1.

Li, Q., Y. Wang, and Y. Duan, 2017: A numerical study of outer rainband formation in a sheared tropical cyclone. *J. Atmos. Sci.*, **74**, 203–227, doi:10.1175/JAS-D-16-0123.1.

Li, Y., K. W. Cheung, and J. C. L. Chan, 2014: Numerical study on the development of asymmetric convection and vertical wind shear during tropical cyclone landfall. *Quart. J. Roy. Meteor. Soc.*, **140**, 1866–1877, doi:10.1002/qj.2259.

Li, Y., Y. Lin, and Y. Wang, 2019: A numerical study on the formation and maintenance of a long-lived rainband in Typhoon Longwang (2005). *J. Geophys. Res.*, **124**, 10401–10426, doi:10.1029/2019JD030600.

Lin, Y.-L., D. B. Ensley, S. Chiao, and C.-Y. Huang, 2002: Orographic influences on rainfall and track deflection associated with the passage of a tropical cyclone. *Mon. Wea. Rev.,* **130,** 2929–2950, doi:10.1175/1520-0493(2002)130<2929:OIORAT>2.0.CO;2.

Lin, Y., Y. Li, Q. Li, M. Chen, F. Xu, Y. Wang, and B. Huang, 2018: A long-lasting vortex Rossby wave–induced rainband of Typhoon Longwang (2005). *Bull. Amer. Meteor. Soc.,* **99**, 1127–1134, doi:10.1175/BAMS-D-17-0122.1.

Liu, M., and J. A. Smith, 2016: Extreme rainfall from landfalling tropical cyclones in the eastern United States: Hurricane Irene (2011). *J. Hydrometeor.*, **17**, 2883–2904, doi:10.1175/ JHM-D-16-0072.1.

Powell, M. D., 1982: The transition of the Hurricane Frederic boundary-layer wind field from the open Gulf of Mexico to landfall. *Mon. Wea. Rev.*, **110**, 1912–1932, doi:10.1175/1520-0493(1982)110,1912:TTOTHF.2.0.CO;2.

Rivera-Torres, N. G., 2018: The impact of high-resolution terrain data on WRF simulation of Hurricane Maria (2017). Non-refereed.

Rotunno, R., J. B. Klemp, and M. L. Weisman, 1988: A theory for strong, long-lived squall lines. *J. Atmos. Sci.*, **45**, 463–485, doi:10.1175/1520-0469(1988)045,0463:ATFSLL.2.0.CO;2.

Skamarock, W. C., and Coauthors, 2008: A description of the Advanced Research WRF version 3. NCAR Tech. Note NCAR/TN-4751STR, 113 pp., doi:10.5065/D68S4MVH.

Smith, R. B., 1979: The influence of mountains on the atmosphere. *Advances in Geophysics*, Vol. 21, Academic Press, 87–230, doi:10.1016/S0065-2687(08)60262-9.

Smith, R. B., P. Schafer, D. Kirshbaum, and E. Regina, 2009: Orographic enhancement of precipitation inside Hurricane Dean. *J. Hydrometeor.,* **10**, 820–831, doi:10.1175/2008JHM1057.1.

Von Storch, H., H. Langenberg, and F. Feser, 2000: A spectral nudging technique for dynamical downscaling purposes. *Mon. Wea. Rev.*, **128**, 3664–3673, doi:10.1175/1520-0493(2000)128h3664:ASNTFDi2.0.CO;2.

Wang, Y., 2002: Vortex Rossby waves in a numerically simulated tropical cyclone. Part I: Overall structure, potential vorticity, and kinetic energy budgets. *J. Atmos. Sci.,* **59**, 1213–1238, doi:10.1175/1520-0469(2002)059<1213:VRWIAN>2.0.CO;2.

Wang, Y., 2008: Rapid filamentation zone in a numerically simulated tropical cyclone. *J. Atmos. Sci.*, **65**, 1158–1181, doi:10.1175/ 2007JAS2426.1.

Wang, Y., and G. J. Holland, 1996: Tropical cyclone motion and evolution in vertical shear. *J. Atmos. Sci.,* **53**, 3313–3332, doi:10.1175/1520-0469(1996)053<3313:TCMAEI>2.0.CO;2.

Xu, W., H. Jiang, and X. Kang, 2014: Rainfall asymmetries of tropical cyclones prior to, during, and after making landfall in South China and Southeast United States. *Atmos. Res*., **139**, 18–26, doi:10.1016/j.atmosres.2013.12.015.

Yu, C.-K., and C.-L. Tsai, 2017: Structural changes of an outer tropical cyclone rainband encountering the topography of northern Taiwan. *Quart. J. Roy. Meteor. Soc*., **143**, 1107–1122, doi:10.1002/qj.2994.

Yu, C.-K., and L.-W. Cheng, 2013: Distribution and mechanisms of orographic precipitation associated with Typhoon Morakot (2009). *J. Atmos. Sci.*, **70**, 2894–2915, doi:10.1175/JAS-D-12-0340.1.

Figure captions

Figure 1. (a) The initial nest configuration (D1, D2, and D3 denote the outermost, second, and innermost domains, respectively), initial (0000 UTC 30 September) surface wind (wind barbs) and sea level pressure (hPa, at an interval of 10 hPa) from dynamical initialization for the simulation studies, overlaid with the 6-hourly IBTrACS best track (Obs) and simulated TC tracks. The orange dashed lines together with the coastline of Mainland China mark the area of interest for the terrain/landmass sensitivity experiments. (b) Temporal evolution of the maximum 10-m wind speed (upper panel, m s^{-1}) and minimum sea level pressure (lower panel, hPa).

Figure 2. (a) The terrain height ASL (m; at a resolution of 12 km) near Fujian within the innermost domain in CTL. Black lines mark the coastlines and provincial boundaries. (b)–(d) Modeled 3-km reflectivity (shading, d*BZ*) and sea level pressure isobars (contour, hPa) at an interval of 10 hPa at 0400, 0800, and 1200 UTC 2 October. Purple dashed concentric circles are 100, 200, and 300 km from the typhoon center. Magenta arrows mark the position of the rainband of interest. (e)–(h) Same as (a)–(d), but from the experiment using the high-resolution terrain dataset with the resolution of terrain height in (e) being 1.33 km.

Figure 3. (a1)–(f1) Doppler radar reflectivity mosaic images (dB*Z*) during 0700–1700 UTC 2 October with the space of blue line being 2^{o} in both latitude and longitude. Magenta arrows mark the position of the rainband of interest. (a2)–(f2), (a3)–(f3), and (a4)–(f4) Evolutions of the simulated rainband during 0200–1200 UTC 2 October in all three experiments as in Figure 2.

Figure 4. The 700-hPa potential vorticity (PVU, 10^{-6} K m^2 kg^{-1} s^{-1}) at 0000 (left column), 0100 (middle column), and 0200 (right column) UTC 2 October in (a)–(c) CTL, (d)–(f) FLT, and (g)–(i) OCN with the black arrows marking the wavenumber-2 potential vorticity band of interest, and black lines marking the coastlines. Purple dashed circles are at every 50 km from the typhoon center.

Figure 5. The 10-h accumulated precipitation (mm) during 0300–1300 UTC 2 October over Fujian province in the three experiments (shading with the 50-mm contour highlighted in cyan) and observations during 0800–1800 UTC 2 October from rain gauge (dot).

Figure 6. The 900-hPa virtual potential temperature (shading, K), 3-km reflectivity (green contours) at 45, 50, and 55 dB*Z*, and deep-layer vertical wind shear between 700 and 200 hPa (black arrow with the shear value printed near the end of the arrow) during 0400–1000 UTC 2 October. Red arrow in (b), (f), and (j) marks the position of the initial surface cold anomaly under the upwind sector of the rainband. Red line near the greatest reflectivity in the upwind sector of the rainband in (c), (d), (g), (h), (k), and (l) marks the segment for the radius-pressure cross section shown in Figure 7. Purple dashed concentric circles are 100, 200, and 300 km from the typhoon center. Black lines mark the coastlines and provincial boundaries

Figure 7. Radius-pressure cross section of the simulated reflectivity (dBZ, shading with the terrain marked as grey), virtual potential temperature perturbation (subtracting the 100-km mean outside the rainband) below 500 hPa (K, contour at an interval of 0.5 K with negative value dashed and zero contour highlighted by cyan), and band-relative secondary circulation (blue vectors) along the red line in Figures 6c,d,g,h,k,l.

Figure 8. Vertically integral-averaged (first integrated and then averaged) horizontal water vapor flux (shading and arrow, g s^{-1} Pa^{-1} m^{-1}), divergence of horizontal water vapor flux (yellow contours, mostly under the red contours, -0.006, -0.005, and -0.004 g s^{-1} Pa^{-1} m^{-2}), and divergence of horizontal wind (red contours, -0.004, -0.003, and -0.002 s^{-1}) between the surface to 1000-m height during 0800–1200 UTC 2 October. Black dashed concentric circles are at 100, 200, and 300 km from the typhoon center, and black solid lines mark the coastlines and provincial boundaries.

Figure 9. (a)–(c): Vertically integral-averaged wind speed (contours, m s^{-1}) and Brunt-Väisälä frequency (shading, 10^{-2} s^{-1}) between the surface to 1000-m height during 0800–1200 UTC 2 October in CTL. (d)–(f) The model's terrain height ASL (shading, m), diagnosed (yellow

contour at 10 [m s^{-1}][g kg^{-1}]) and simulated (red contours at 30, 40, and 50 [m s^{-1}][g kg^{-1}]) 1000-m upward water vapor flux, and 3-km reflectivity (purple contours at 45, 50, and 55 dB*Z*) during 0800–1200 UTC 2 October in CTL. Black dashed concentric circles in (a)–(f) are at 100, 200, and 300 km from the typhoon center, and black light solid lines mark the coastlines and provincial boundaries. (g)–(i) Vertical structure of vertical velocity (shading, m s^{-1}) and transverse circulation (arrows) along the black thick solid line segments in (d)–(f), respectively, with the terrain marked as grey shading.

Figure 10. (a)–(c) Vertically integral-averaged radial component of the horizontal water vapor flux (shading, g s^{-1} Pa^{-1} m^{-1}) and the corresponding radial divergence (contours, -0.004, -0.003, and -0.002 g s^{-1} Pa^{-1} m^{-2}) between the surface to 1000-m height during 0800–1200 UTC 2 October in CTL. Black dashed concentric circles are at 100, 200, and 300 km from the typhoon center, and black solid lines mark the coastlines and provincial boundaries. (d)–(f) Same as (a)–(c), but for the tangential component of the horizontal water vapor flux and the corresponding tangential divergence.

Figure 11. Vertically integral-averaged vertical diffusion (mixing) of tangential wind (including surface friction) between the surface to 1000-m height (shading, m s^{-1} h^{-1}) and 3-km reflectivity (contours) at 45, 50, and 55 dB*Z* during 0800–1200 UTC 2 October. Black dashed concentric circles are at 100, 200, and 300 km from the typhoon center, and black solid lines mark the coastlines and provincial boundaries. Magenta rectangle marks the upwind sector of the rainband near the coastline.

Figure 12. (a)–(c) Vertically integral-averaged tangential wind speed between 850–1000 hPa (shading, m s^{-1}) and 3-km reflectivity (contours) at 45, 50, and 55 dB*Z* at 1000 UTC 2 October within the magenta rectangle of Figures 11b,e,h. Dashed red line marks the reduction of tangential wind over land in the front of the rainband. Black solid lines mark the coastlines. (d)–(f) Same as (a)–(c), but the shading shows the vertically integral-averaged agradient force (m s^{-1} h^{-1}). Dashed cyan line marks the location of the main radially inward agradient force in

the front of the rainband. (g)–(i) Same as (d)–(f), but the shading shows the vertically integral-averaged vertical mixing including surface friction of radial wind (m s^{-1} h^{-1}). Magenta arrows mark the position of the rainband of interest. (j)–(l) Same as (a)–(c), but the shading shows the vertically integral-averaged radial velocity (m s^{-1}).

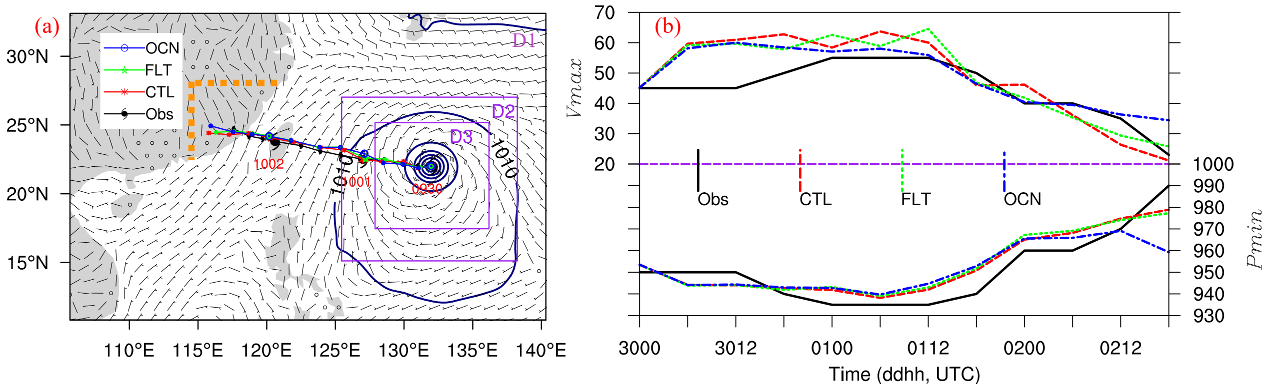

Figure 1. (a) The initial nest configuration (D1, D2, and D3 denote the outermost, second, and innermost domains, respectively), initial (0000 UTC 30 September) surface wind (wind barbs) and sea level pressure (hPa, at an interval of 10 hPa) from dynamical initialization for the simulation studies, overlaid with the 6-hourly IBTrACS best track (Obs) and simulated TC tracks. The orange dashed lines together with the coastline of Mainland China mark the area of interest for the terrain/landmass sensitivity experiments. (b) Temporal evolution of the maximum 10-m wind speed (upper panel, m s^{-1}) and minimum sea level pressure (lower panel, hPa).

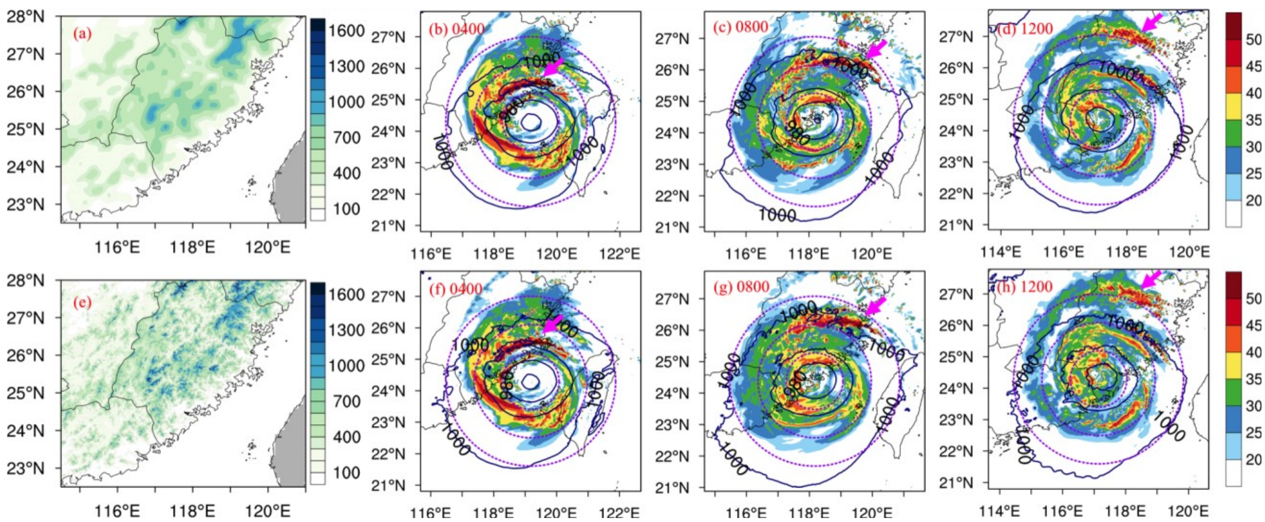

Figure 2. (a) The terrain height ASL (m; at a resolution of 12 km) near Fujian within the innermost domain in CTL. Black lines mark the coastlines and provincial boundaries. (b)–(d) Modeled 3-km reflectivity (shading, dB*Z*) and sea level pressure isobars (contour, hPa) at an interval of 10 hPa at 0400, 0800, and 1200 UTC 2 October. Purple dashed concentric circles are 100, 200, and 300 km from the typhoon center. Magenta arrows mark the position of the rainband of interest. (e)–(h) Same as (a)–(d), but from the experiment using the high-resolution terrain dataset with the resolution of terrain height in (e) being 1.33 km.

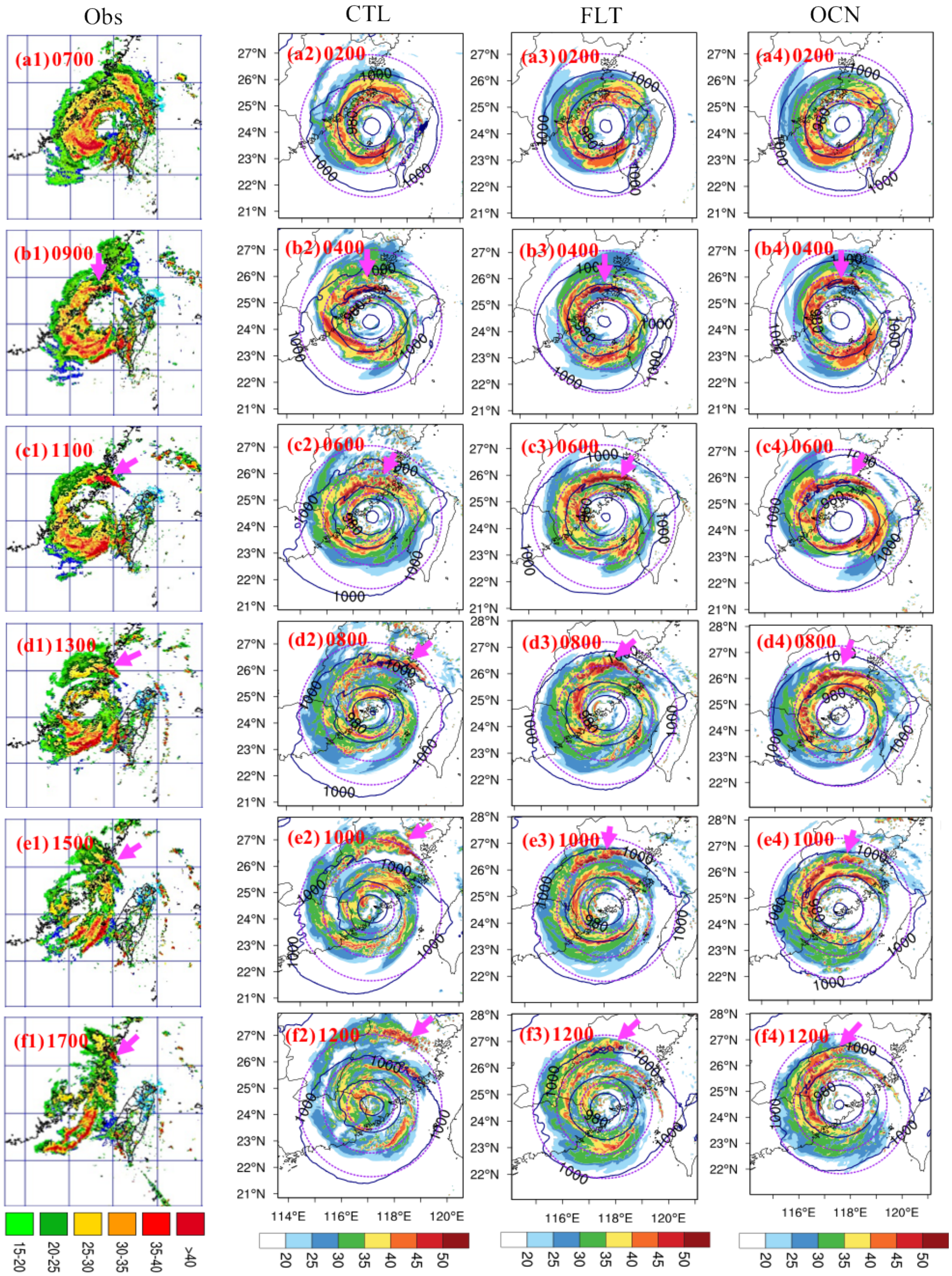

Figure 3. (a1)–(f1) Doppler radar reflectivity mosaic images (dB*Z*) during 0700–1700 UTC 2 October with the space of blue line being 2º in both latitude and longitude. Magenta arrows mark the position of the rainband of interest. (a2)–(f2), (a3)–(f3), and (a4)–(f4) Evolutions of the simulated rainband during 0200–1200 UTC 2 October in all three experiments as in Figure 2.

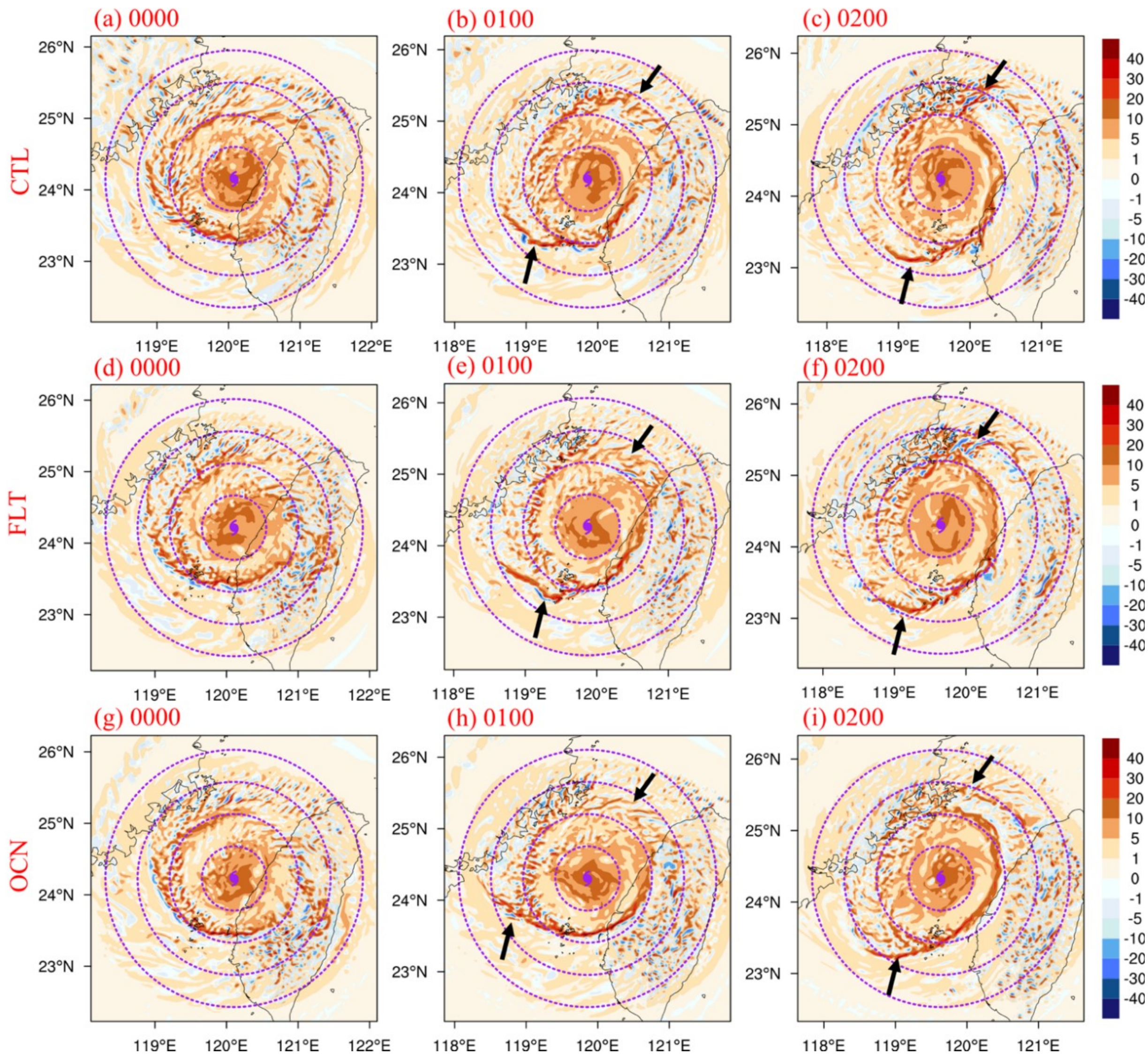

Figure 4. The 700-hPa potential vorticity (PVU, 10^{-6} K m^2 kg^{-1} s^{-1}) at 0000 (left column), 0100 (middle column), and 0200 (right column) UTC 2 October in (a)–(c) CTL, (d)–(f) FLT, and (g)–(i) OCN with the black arrows marking the wavenumber-2 potential vorticity band of interest, and black lines marking the coastlines. Purple dashed circles are at every 50 km from the typhoon center.

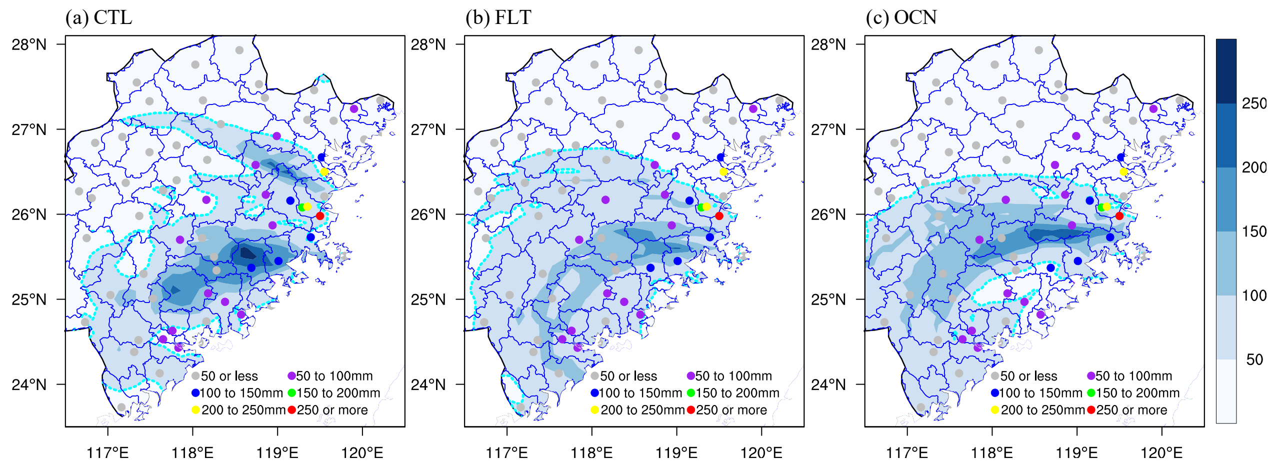

Figure 5. The 10-h accumulated precipitation (mm) during 0300–1300 UTC 2 October over Fujian province in the three experiments (shading with the 50-mm contour highlighted in cyan) and observations during 0800–1800 UTC 2 October from rain gauge (dot).

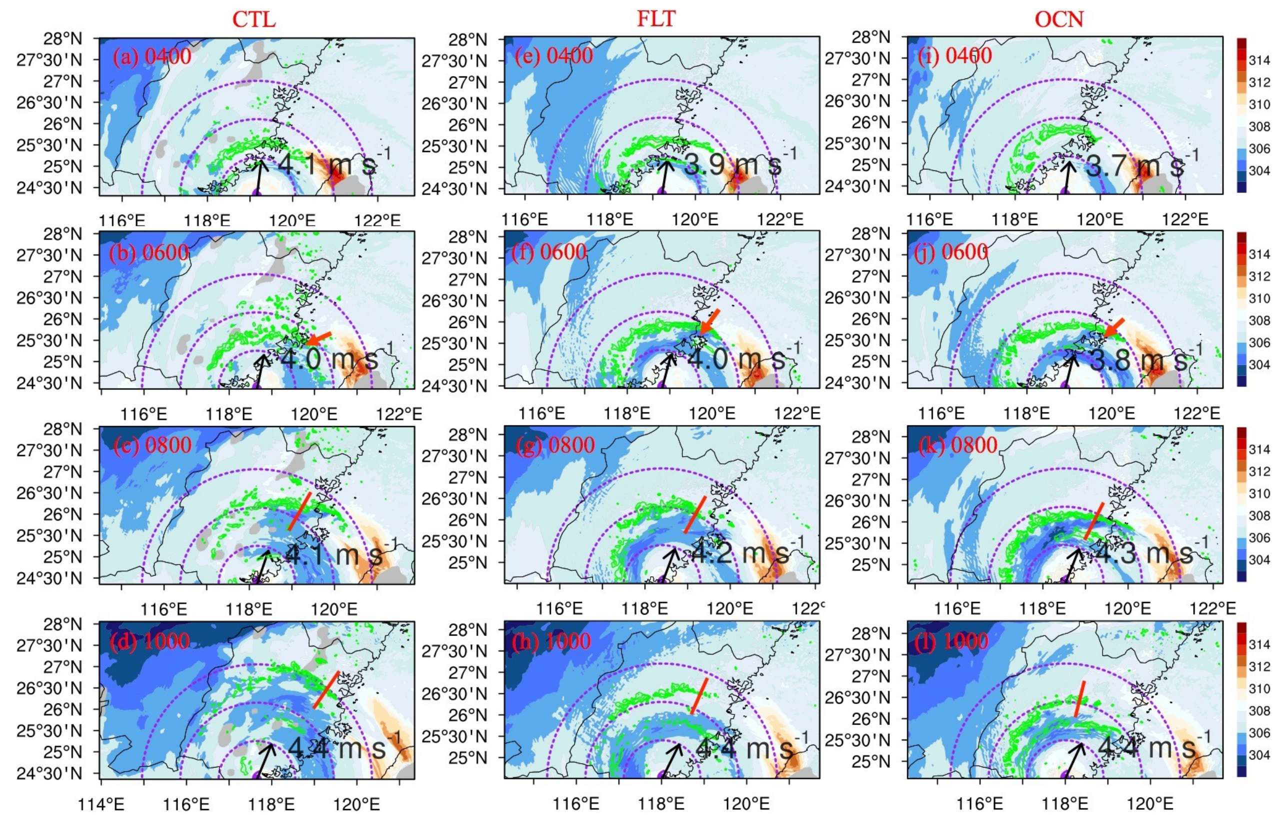

Figure 6. The 900-hPa virtual potential temperature (shading, K), 3-km reflectivity (green contours) at 45, 50, and 55 dB*Z*, and deep-layer vertical wind shear between 700 and 200 hPa (black arrow with the shear value printed near the end of the arrow) during 0400–1000 UTC 2 October. Red arrow in (b), (f), and (j) marks the position of the initial surface cold anomaly under the upwind sector of the rainband. Red line near the greatest reflectivity in the upwind sector of the rainband in (c), (d), (g), (h), (k), and (l) marks the segment for the radius-pressure cross section shown in Figure 7. Purple dashed concentric circles are 100, 200, and 300 km from the typhoon center. Black lines mark the coastlines and provincial boundaries.

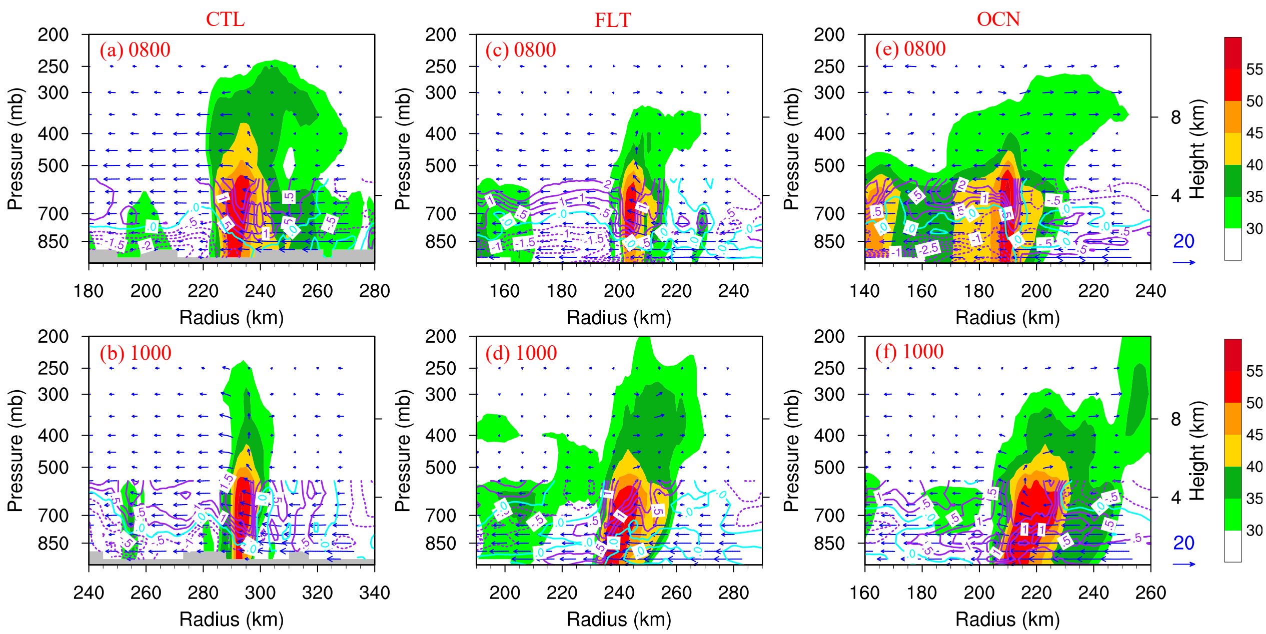

Figure 7. Radius-pressure cross section of the simulated reflectivity (dBZ, shading with the terrain marked as grey), virtual potential temperature perturbation (subtracting the 100-km mean outside the rainband) below 500 hPa (K, contour at an interval of 0.5 K with negative value dashed and zero contour highlighted by cyan), and band-relative secondary circulation (blue vectors) along the red line in Figures 6c,d,g,h,k,l.

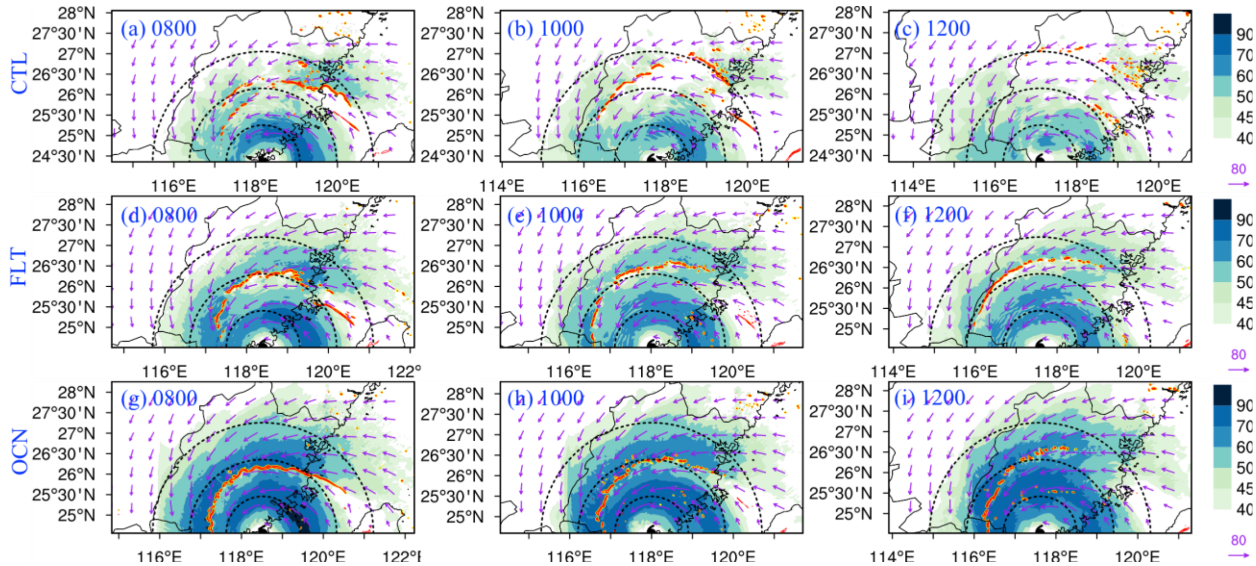

Figure 8. Vertically integral-averaged (first integrated and then averaged) horizontal water vapor flux (shading and arrow, g s^{-1} Pa^{-1} m^{-1}), divergence of horizontal water vapor flux (yellow contours, mostly under the red contours, -0.006, -0.005, and -0.004 g s^{-1} Pa^{-1} m^{-2}), and divergence of horizontal wind (red contours, -0.004, -0.003, and -0.002 s^{-1}) between the surface to 1000-m height during 0800–1200 UTC 2 October. Black dashed concentric circles are at 100, 200, and 300 km from the typhoon center, and black solid lines mark the coastlines and provincial boundaries.

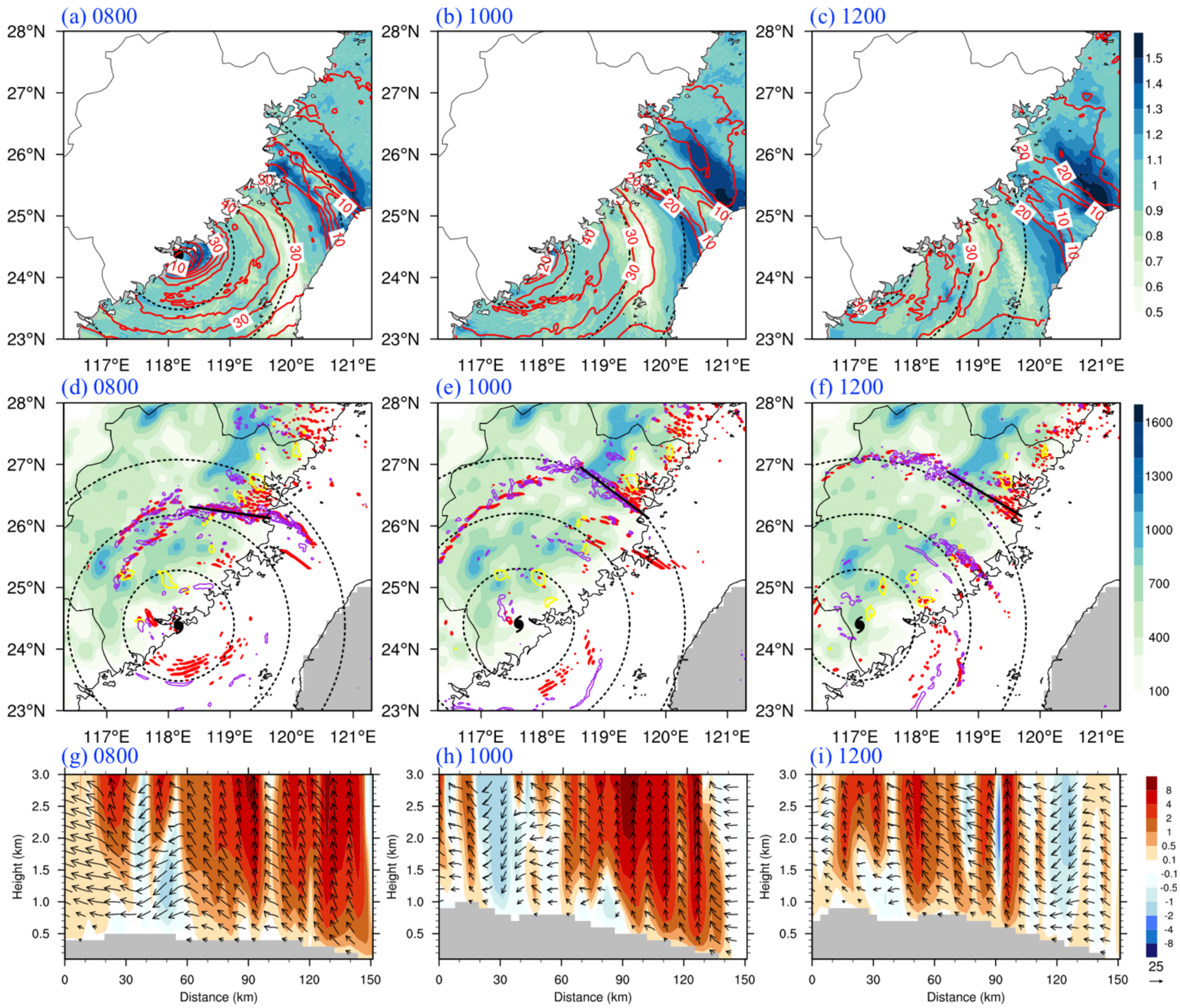

Figure 9. (a)–(c): Vertically integral-averaged wind speed (contours, m s^{-1}) and Brunt-Väisälä frequency (shading, 10^{-2} s^{-1}) between the surface to 1000-m height during 0800–1200 UTC 2 October in CTL. (d)–(f) The model's terrain height ASL (shading, m), diagnosed (yellow contour at 10 [m s^{-1}][g kg $^{-1}$]) and simulated (red contours at 30, 40, and 50 [m s^{-1}][g kg $^{-1}$]) 1000-m upward water vapor flux, and 3-km reflectivity (purple contours at 45, 50, and 55 dB*Z*) during 0800–1200 UTC 2 October in CTL. Black dashed concentric circles in (a)–(f) are at 100, 200, and 300 km from the typhoon center, and black light solid lines mark the coastlines and provincial boundaries. (g)–(i) Vertical structure of vertical velocity (shading, m s^{-1}) and transverse circulation (arrows) along the black thick solid line segments in (d)–(f), respectively, with the terrain marked as grey shading.

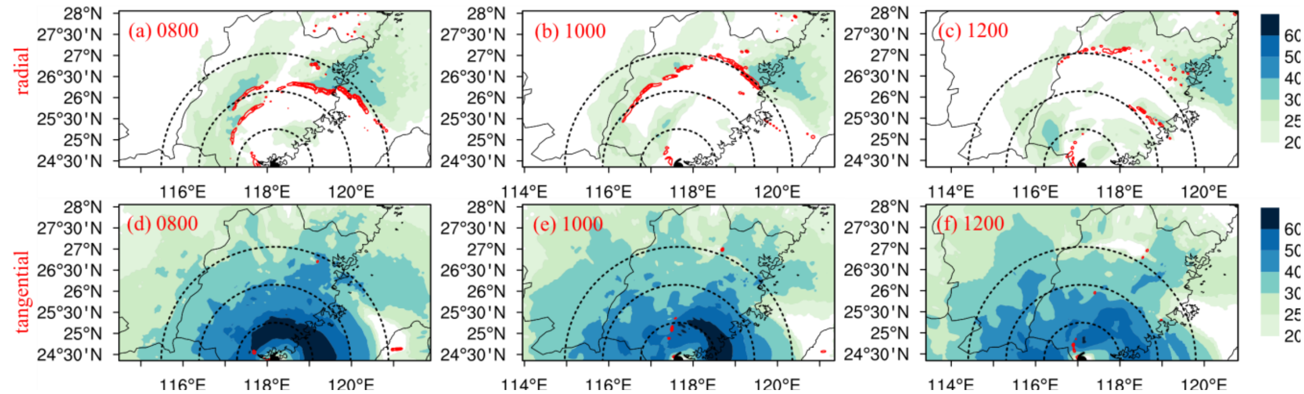

Figure 10. (a)–(c) Vertically integral-averaged radial component of the horizontal water vapor flux (shading, g s^{-1} Pa^{-1} m^{-1}) and the corresponding radial divergence (contours, -0.004, -0.003, and -0.002 g s^{-1} Pa^{-1} m^{-2}) between the surface to 1000-m height during 0800–1200 UTC 2 October in CTL. Black dashed concentric circles are at 100, 200, and 300 km from the typhoon center, and black solid lines mark the coastlines and provincial boundaries. (d)–(f) Same as (a)–(c), but for the tangential component of the horizontal water vapor flux and the corresponding tangential divergence.

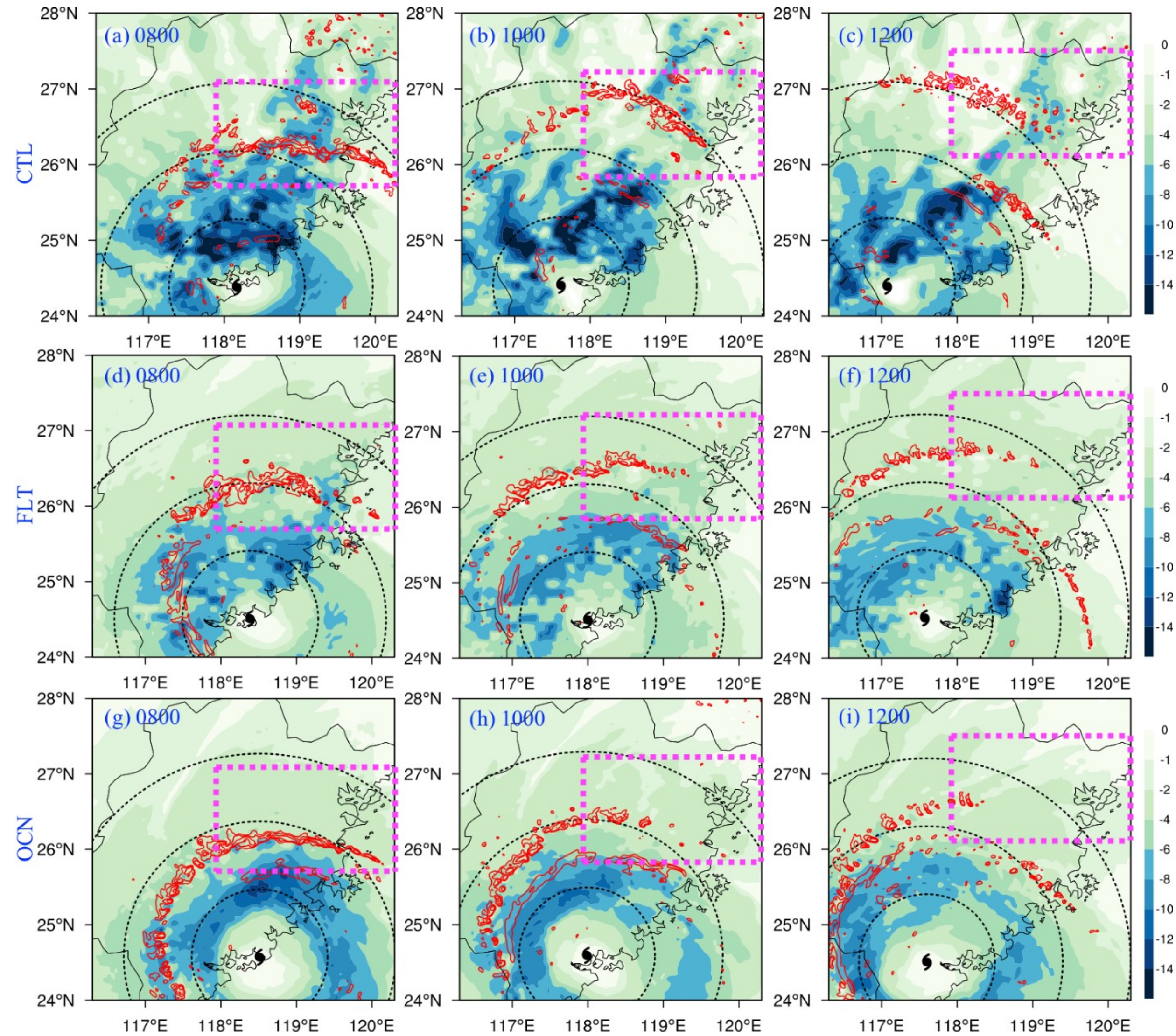

Figure 11. Vertically integral-averaged vertical diffusion (mixing) of tangential wind (including surface friction) between the surface to 1000-m height (shading, m s^{-1} h^{-1}) and 3-km reflectivity (contours) at 45, 50, and 55 d*BZ* during 0800–1200 UTC 2 October. Black dashed concentric circles are at 100, 200, and 300 km from the typhoon center, and black solid lines mark the coastlines and provincial boundaries. Magenta rectangle marks the upwind sector of the rainband near the coastline.

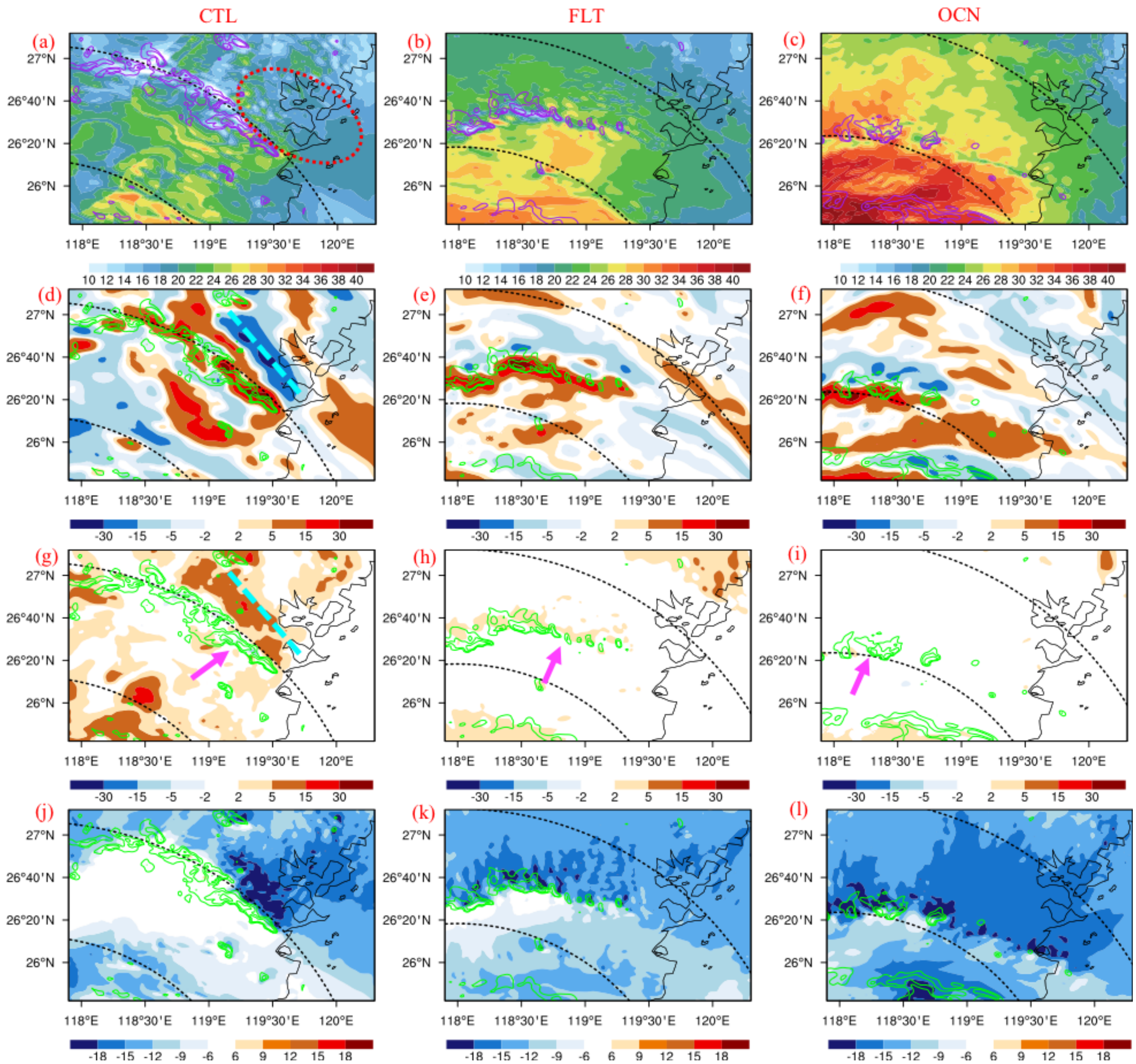

Figure 12. (a)–(c) Vertically integral-averaged tangential wind speed between 850–1000 hPa (shading, m s^{-1}) and 3-km reflectivity (contours) at 45, 50, and 55 dB*Z* at 1000 UTC 2 October within the magenta rectangle of Figures 11b,e,h. Dashed red line marks the reduction of tangential wind over land in the front of the rainband. Black solid lines mark the coastlines. (d)–(f) Same as (a)–(c), but the shading shows the vertically integral-averaged agradient force (m s^{-1} h^{-1}). Dashed cyan line marks the location of the main radially inward agradient force in the front of the rainband. (g)–(i) Same as (d)–(f), but the shading shows the vertically integral-averaged vertical mixing including surface friction of radial wind (m s^{-1} h^{-1}). Magenta arrows mark the position of the rainband of interest. (j)–(l) Same as (a)–(c), but the shading shows the vertically integral-averaged radial velocity (m s^{-1}).